

## REVIEW

[View Article Online](#)  
[View Journal](#) | [View Issue](#)Cite this: *Nanoscale Adv.*, 2024, 6, 6096Photocatalytic deposition of noble metals on 0D, 1D, and 2D TiO<sub>2</sub> structures: a reviewSalih Veziroglu,<sup>ID</sup>\*<sup>ab</sup> Josiah Shondo,<sup>a</sup> Tim Tjardts,<sup>a</sup> Tamim B. Sarwar,<sup>a</sup> Ayse Sünbül,<sup>ac</sup> Yogendra Kumar Mishra,<sup>ID</sup><sup>d</sup> Franz Faupel<sup>ID</sup><sup>ab</sup> and Oral Cenk Aktas<sup>ID</sup>\*<sup>a</sup>

In recent years, extensive research on noble metal–TiO<sub>2</sub> nanocomposites has demonstrated their crucial role in various applications such as water splitting, self-cleaning, CO<sub>2</sub> reduction, and wastewater treatment. The structure of the noble metal–TiO<sub>2</sub> nanocomposites is critical in determining their photocatalytic properties. Numerous studies in the literature describe the preparation of these nanocomposites with various shapes and sizes to achieve tunable photocatalytic performance. However, achieving a stable coupling between the noble metal and the TiO<sub>2</sub> surface remains a challenge for long-term use. Photocatalytic deposition is one of the most promising approaches to obtain well-defined noble metal structures on TiO<sub>2</sub> surfaces with strong adhesion. Noble metal nanoparticles (NPs) can be quickly grown on the TiO<sub>2</sub> surface under light exposure. However, various parameters such as the pH, temperature, precursor, and electron sacrificial agent affect the size and distribution of the deposited particles. In this review article, we look at the critical parameters that influence the photocatalytic deposition of noble metals on major TiO<sub>2</sub> morphologies, classified as 0D (NPs and nanocrystals), 1D (nanotubes and nanowires), and 2D (thin films).

Received 28th July 2024  
Accepted 4th November 2024

DOI: 10.1039/d4na00623b

[rsc.li/nanoscale-advances](http://rsc.li/nanoscale-advances)

## 1 Introduction

Over the last few decades, nanomaterials have attracted exceptional research interest due to their unique physical and chemical properties, mainly arising from their high surface area (enormous surface-to-volume ratios) and nanoscale size.<sup>1</sup> Among the different kinds of nanomaterials, noble metal (Au, Ag, Pt, Pd, as well as the Au/Ag alloy) and metal oxide (TiO<sub>2</sub>, ZnO, Cu<sub>2</sub>O, and CeO<sub>2</sub>) nanocomposites with well-defined structures and properties have gained significant attention for many applications, especially in photocatalysis<sup>2</sup> (degradation of organic pollutants,<sup>3</sup> photocatalytic hydrogen generation, photocatalytic CO<sub>2</sub> reduction, *etc.*), solar cells,<sup>4</sup> biomedicine<sup>5</sup> and surface-enhanced Raman spectroscopy (SERS) (Fig. 1).<sup>6,7</sup> The effectiveness of these hybrid nanocomposites depends highly on their size,<sup>8</sup> shape,<sup>4</sup> and structure-dependent properties (*e.g.*, surface and interface chemistry).<sup>9</sup> Therefore, the rational design (new structures with specific functionality), well-controlled synthesis and detailed characterization, and a better

understanding of structure–property relationships are crucial to the functionality of the nanocomposites and their use in real-world applications.<sup>10</sup>

In the literature, several methods exist to prepare functional noble metal–metal oxide nanostructures, including impregnation,<sup>11</sup> chemical vapor deposition,<sup>12</sup> solvothermal synthesis,<sup>13</sup> electrodeposition,<sup>14</sup> atomic-layer deposition (ALD),<sup>15</sup> sputtering,<sup>16</sup> physical mixing,<sup>12</sup> and green synthesis<sup>17</sup> (Table 1). Among these methods, photocatalytic deposition (photodeposition or

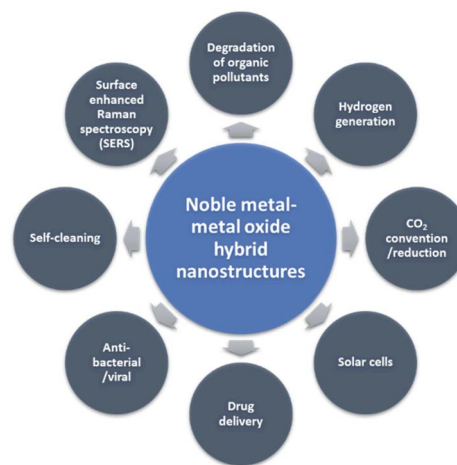


Fig. 1 General applications of noble metal–metal oxide hybrid nanostructures.

<sup>a</sup>Chair for Multicomponent Materials, Department of Materials Science, Faculty of Engineering, Kiel University, Kaiserstr. 2, 24143 Kiel, Germany. E-mail: [sve@tf.uni-kiel.de](mailto:sve@tf.uni-kiel.de); [oca@tf.uni-kiel.de](mailto:oca@tf.uni-kiel.de)

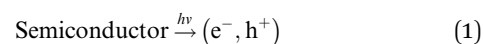
<sup>b</sup>Kiel Nano, Surface and Interface Science KiNSIS, Kiel University, Christian Albrechts-Platz 4, 24118, Kiel, Germany

<sup>c</sup>Fraunhofer Institute for Photonic Microsystems IPMS, Center Nanoelectronic Technologies CNT, An der Bartlake 5, Dresden, 01109, Germany

<sup>d</sup>Mads Clausen Institute, NanoSYD, University of Southern Denmark, Alsion 2, 6400 Sønderborg, Denmark

Method	Advantages	Disadvantages
Photodeposition	<ul style="list-style-type: none"> <li>• Mild reaction conditions</li> <li>• Low cost and simple setup</li> <li>• Green and safe process</li> <li>• Control over spatial distribution of nanoparticles</li> <li>• Potential for various applications (photocatalysis, electrocatalysis, <i>etc.</i>)</li> </ul>	<ul style="list-style-type: none"> <li>• Requires specific light conditions (<i>e.g.</i>, UV)</li> <li>• Limited to certain metals and substrates</li> <li>• May have lower deposition rates compared to other methods</li> </ul>
Simple reduction process	<ul style="list-style-type: none"> <li>• Low-cost and straightforward method</li> </ul>	<ul style="list-style-type: none"> <li>• Often requires additional reducing agents unless spontaneous reduction is used</li> <li>• Control over particle size can be limited</li> </ul>
Chemical vapor deposition (CVD)	<ul style="list-style-type: none"> <li>• Can be performed under ambient conditions</li> <li>• Minimal equipment required</li> <li>• High purity and uniformity of films</li> <li>• Suitable for large-scale production</li> </ul>	<ul style="list-style-type: none"> <li>• High temperatures required</li> <li>• Complex equipment setup</li> <li>• Potentially hazardous chemicals involved</li> </ul>
Sputtering	<ul style="list-style-type: none"> <li>• Good control over thickness</li> <li>• Versatile for different materials</li> <li>• Good adhesion to substrates</li> <li>• Can produce thin films with controlled thickness</li> </ul>	<ul style="list-style-type: none"> <li>• Requires vacuum conditions</li> <li>• Can lead to non-uniform coatings</li> <li>• Equipment can be expensive</li> </ul>
Electrochemical deposition	<ul style="list-style-type: none"> <li>• Low cost and simple setup</li> <li>• Good control over morphology and composition</li> <li>• Can be done at room temperature</li> </ul>	<ul style="list-style-type: none"> <li>• Limited to conductive substrates</li> <li>• May require post-deposition treatments for optimal properties</li> </ul>
Laser ablation	<ul style="list-style-type: none"> <li>• High control over particle size and shape</li> <li>• Fast processing times</li> <li>• Minimal contamination risk</li> </ul>	<ul style="list-style-type: none"> <li>• Expensive equipment needed</li> <li>• Limited scalability for mass production</li> </ul>
Atomic layer deposition (ALD)	<ul style="list-style-type: none"> <li>• Atomic-level control over thickness and composition</li> <li>• Excellent uniformity on complex surfaces</li> </ul>	<ul style="list-style-type: none"> <li>• Slow deposition rates</li> <li>• High cost of precursors and equipment</li> </ul>

energy promotes an electron from the valence band to the conduction band, creating an electronic vacancy or “hole” ( $h^+$ ) in the valence band (see eqn (1)).<sup>24</sup>



Typically, the energy level at the bottom of the conduction band determines the reducing ability of the photoelectrons, while the energy level at the top of the valence band determines the oxidizing ability of the photogenerated holes.<sup>25</sup> Both of these species can be utilized in photocatalytic redox reactions. Normally, the conduction band electrons facilitate reduction reactions with the surrounding chemical species, while the valence band holes provide electron acceptors for photocatalytic oxidation.<sup>23</sup> This understanding is critical for designing metal-supported catalysts *via* the photodeposition technique. For a successful photocatalytic reduction, the photocatalyst's conduction band edge should be more negative than the reduction reaction's standard potential on the NHE scale.<sup>23</sup> Conversely, for successful photocatalytic oxidation, the valence band edge must be more positive than the corresponding reduction's standard potential. Photodeposition relies on photocatalytic redox reactions with precursor species, which is schematically shown in Fig. 2. In the photodeposition of metals, the corresponding generalized reduction reaction from a metal precursor ion  $M^{n+}$  reduced by  $n$  conduction band electrons is given in eqn (2).<sup>23</sup>

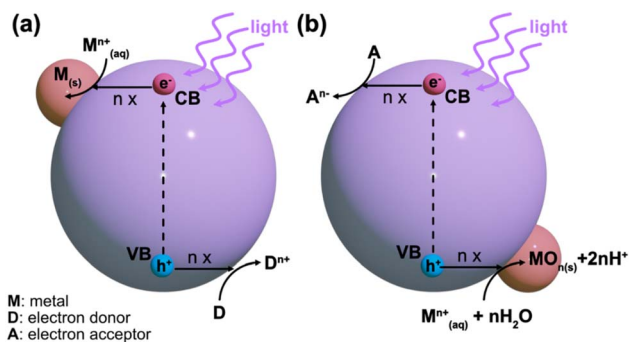
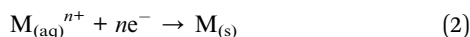


Fig. 2 Schematic illustration of (a) reductive and (b) oxidative photo-deposition processes.



Alternatively, in an oxidative counterpart reaction with  $n$  valence band holes and water, a metal oxide species is formed, as shown in eqn (3)<sup>23</sup>



When a metal particle with a higher work function is in contact with an n-type semiconductor, electrons transfer from the semiconductor to the metal particle.<sup>26,27</sup> Consequently, at the metal–semiconductor interface, a rectifying Schottky barrier is formed.<sup>28</sup> This barrier facilitates charge separation by reducing the electron–hole recombination, thereby enhancing the photocatalytic activity of materials like TiO<sub>2</sub>.<sup>29</sup> Because of the improved separation of electrons and holes, metal deposition on the semiconductor surface enhances photocatalytic reactions by hastening the transfer of electrons to reactants, such as dissolved oxygen molecules.<sup>30</sup> The prediction of Schottky barrier formation and overall band structure typically relies on literature-reported or experimentally determined work functions as a starting point. However, the work function of metal oxide semiconductors like TiO<sub>2</sub> is highly sensitive to experimental conditions, leading to a wide range of reported values.<sup>31,32</sup> Moreover, the work functions can vary depending on factors such as crystallinity, particle geometry<sup>33,34</sup> and the surrounding environment.<sup>32</sup> This makes accurate predictions of band structure and Schottky barrier formation challenging as these properties are influenced by the crystal structure, morphology and the operational environment.

Among many semiconductor materials, TiO<sub>2</sub> is one of the most suitable candidates for industrial applications due to its photoactivity, high chemical stability, eco-friendliness, and cost effectiveness. However, it has two drawbacks restricting its photocatalytic applications: limited photoresponse range ( $\lambda < 380$  nm) and low quantum yields at longer wavelengths ( $\lambda > 400$  nm). The quantum yield increases upon modification of the TiO<sub>2</sub> surface with noble metals such as Au, Ag, Pt, and Pd due to the formation of a Schottky contact.<sup>20</sup> Moreover, when the TiO<sub>2</sub> surface is modified with noble metals, it can lead to a shift in the absorption edge of the TiO<sub>2</sub> to the vis region (narrowing

band gap). Also, localized surface plasmonic activity of the noble metals boosts the excitation of active charge carriers.<sup>35</sup> Due to these synergetic effects of noble metals and TiO<sub>2</sub>, an enhancement in the photocatalytic activity is achieved, providing an excellent opportunity for industrial use under solar light illumination.<sup>36</sup> Hence, photocatalytic deposition of noble metals and metal oxides on TiO<sub>2</sub> has gained more attention in recent years because of its applications in photocatalytic solar fuel synthesis,<sup>37</sup> wastewater treatment,<sup>38</sup> air purification,<sup>24</sup> self-cleaning,<sup>39,40</sup> and biomedical applications.<sup>41</sup>

Photoinduced redox reactions at the surface of TiO<sub>2</sub> have been known since the early 20th century. In 1920/21, Carl Renz reported observations of the darkening effect of TiO<sub>2</sub> when exposed to sunlight.<sup>42</sup> Later, it was shown that photoreactions with the surrounding medium, including exposure of TiO<sub>2</sub> to light in the presence of silver nitrate (AgNO<sub>3</sub>), resulted in the reduction of AgNO<sub>3</sub> to metallic Ag (deposition of Ag particles).<sup>43</sup> A few decades later, Clark and Vondjic reported infrared spectroscopy studies of TiO<sub>2</sub> NPs mixed with AgNO<sub>3</sub>. They showed that AgNO<sub>3</sub> was reduced to metallic Ag after UV irradiation of the mixture.<sup>44</sup> However, the study, which was reported by Kraeutler and Bard in 1978, sparked much research interest in the photodeposition process.<sup>45</sup> In this report, platinum (Pt) was photodeposited on TiO<sub>2</sub> (anatase) by irradiating a paste containing anatase powder, hexachloroplatinic acid (H<sub>2</sub>PtCl<sub>6</sub>), hydrochloric acid (HCl), sodium carbonate (Na<sub>2</sub>CO<sub>3</sub>), and acetic acid (CH<sub>3</sub>COOH) as an electron scavenger. During the reaction process, the system was purged with nitrogen to remove O<sub>2</sub> and CO<sub>2</sub>, and the temperature was increased to 55 °C. Finally, it was shown that well-dispersed Pt NPs could be obtained *via* photodeposition.

The photodeposition process has been known for more than 55 years in the scientific community. However, it is still a challenge to understand all process parameters to obtain well-desired structures for specific applications since several parameters need to be considered to allow the photodeposition process to occur on the semiconductor surface, such as the sacrificial reagent,<sup>46</sup> pH,<sup>47</sup> temperature,<sup>48</sup> metal precursor,<sup>49</sup> light exposure time<sup>50</sup> and intensity,<sup>51</sup> and absence or presence of oxygen in the media.<sup>23</sup> To date, many research and review articles have concentrated on the effect of such photodeposition parameters, especially using TiO<sub>2</sub>.<sup>23,52–54</sup> Only a few studies have focused on investigating the impact of the morphology of TiO<sub>2</sub> on the photodeposition process, unlike other deposition parameters. The morphology directly influences the photodeposition process by affecting the specific/active surface area, availability of charge carriers, pore structure, crystalline phase, and exposed surface facet.<sup>55,56</sup> Therefore, the morphology differences need to be considered as one of the key points to achieve well-desired photodeposited nanostructures on the TiO<sub>2</sub> surface. As depicted in Fig. 3, variable morphologies of TiO<sub>2</sub> are categorized as 0D: NPs and nanocrystals; 1D: nanotubes and nanowires; and 2D: thin films.

So far, numerous research articles have reported on the preparation of noble metals on TiO<sub>2</sub> surfaces *via* photodeposition, highlighting the advantages of this approach.<sup>46,52,57,58</sup> Additionally, excellent reviews have been



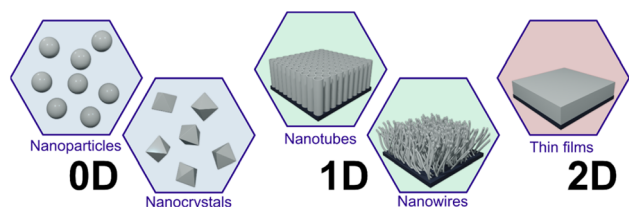


Fig. 3 Schematic illustration of the most used TiO<sub>2</sub> morphologies (0D: NPs and nanocrystals; 1D: nanotubes and nanowires; and 2D: thin films).

published in the past few years on the photodeposition process that focused on the methods, mechanisms, and applications of photodeposition.<sup>23,59</sup> In most cases, the authors have focused on the effect of deposition parameters, which include the sacrificial electron donors, pH, precursor, temperature, as well as the absence and presence of oxygen.<sup>23,59,60</sup> However, a comprehensive review analyzing the role of various TiO<sub>2</sub> morphologies in the catalytic activity and photodeposition processes is still lacking, hindering further advancement in photocatalytic research. Therefore, in this review article, we provide an overview of the recent research progress on the photodeposition of noble metals on different TiO<sub>2</sub> morphologies such as 0D: NPs and nanocrystals; 1D: nanotubes and nanowires; and 2D: thin films. The following sections can give researchers different perspectives on the photodeposition process based on used materials and systems. Additionally, future perspectives on preparing future metal–semiconductor systems *via* photodeposition will be presented and discussed.

## 2 Photocatalytic deposition of noble metal nanoparticles on different TiO<sub>2</sub> morphologies

### 2.1. 0D structures

**2.1.1. TiO<sub>2</sub> nanoparticles.** 0D structures refer to materials with all dimensions confined to the nanoscale, typically below 100 nanometers. These structures often take the form of nanoparticles, which can exhibit unique physical and chemical properties due to their small size and high surface-to-volume ratio. Common examples of 0D nanomaterials include nanoparticles, quantum dots, and fullerenes. As is known, Degussa P25 (*ca.* 70–80% anatase and 30–20% rutile) is the brand name of TiO<sub>2</sub> NPs widely used in photocatalytic reactions due to its relatively high photoreactivity. It is difficult to find a photocatalyst that has an activity that is higher than the activity of P25 TiO<sub>2</sub>.<sup>61</sup> Therefore, P25 TiO<sub>2</sub> has been used as a *de facto* standard titania photocatalyst. Hence, since the 1900s, more than a thousand articles have been reported on the P25 TiO<sub>2</sub> photocatalytic reactions.<sup>62</sup> The phase composition of Degussa Evonik P25 is not clearly defined, as the exact ratios of anatase and rutile can vary depending on production methods and conditions.<sup>63</sup> However, Table 2 reveals other essential properties of P25 TiO<sub>2</sub> based on the information supplied by Evonik (Evonik Research Efficiency GmbH, 2020).<sup>64</sup>

Table 2 Summary of specific properties of P25 TiO<sub>2</sub> (ref. 64)

Properties	Units	Value
Specific surface area	m <sup>2</sup> g <sup>−1</sup>	35–65
Approximate particle size <sup>64</sup>	Nm	20
pH value in 4% dispersion	—	3.5–4.5
Tapped density	g L <sup>−1</sup>	100–180

Research groups have provided detailed insights into the phase structure of P25 TiO<sub>2</sub>. It has been established that P25 TiO<sub>2</sub> powder comprises multiphasic TiO<sub>2</sub> nanoparticles (NPs), consisting of approximately 80% anatase and 20% rutile in the crystalline phase. Additionally, an amorphous phase has been identified through X-ray diffraction (XRD) analysis and transmission electron microscopy (TEM) measurements.<sup>64</sup> It has been determined that the anatase to rutile ratio changes from batch to batch and should be somewhere between 70 : 30 and 80 : 20.<sup>65</sup>

P25 TiO<sub>2</sub> has been frequently used as a substrate material for the photodeposition of noble metals, among other TiO<sub>2</sub> NPs.<sup>30,46,58,67,68</sup> Sclafani and Herrmann first demonstrated the growth of noble metals on P25 TiO<sub>2</sub> in 1998.<sup>69</sup> They reported the effect of grown Ag nanoparticles on the photocatalytic activity of TiO<sub>2</sub>, specifically rutile and anatase phases in both organic and aqueous media. Ag–P25 TiO<sub>2</sub> samples were prepared *via* photocatalytic deposition by irradiating an aqueous AgNO<sub>3</sub> solution with a 125 W high-pressure mercury lamp, using a 300 nm optical filter.<sup>69</sup> Furthermore, the authors investigated the effect of deposited noble metals (Ag and Pt) as both single and bimetallic systems on the distinctive phases of P25. Notably, in the anatase phase, Pt selectively grows atop pre-existing Ag particles, showing 100% selectivity. Whereas, in the rutile phase, Pt can grow both on Ag particles and directly on the rutile surface. Additionally, the study showed that Ag deposits are beneficial for rutile activity but has detrimental effect on anatase activity.<sup>69</sup>

Over the past few decades, the photodeposition of noble metals on commercial P25 TiO<sub>2</sub> has been investigated to improve control over the particle size, distribution, and morphology for specific applications.<sup>58,66</sup> In this regard, Bhardwaj *et al.* studied the effects of different wt% of Ag loadings on commercial P25 TiO<sub>2</sub> and different deposition times (30–90 min) on the structural, optical, and photocatalytic properties of Ag/TiO<sub>2</sub> nanocomposites. The study showed that increasing the loading amount and UV irradiation time during photodeposition enhanced the plasmonic response, resulting in uniform nanostructure growth and regular distribution of Ag NPs.<sup>58</sup>

Pt is the most effective metal catalyst in conventional thermal oxidation processes among other noble metals. In particular, the loading of Pt onto the P25 TiO<sub>2</sub> surface increases the efficiency of charge separation and promotes the amount of absorbed organic compound on the surface. Platinum (Pt) functions as an electron sink through the formation of a charge-transfer complex with TiO<sub>2</sub>. The catalytic properties of Pt are particularly influenced by several factors, including the





nanoparticle size, dispersion, morphology, and oxidation state.<sup>52</sup> Jiang *et al.*<sup>66</sup> showed that methanol is critical for controlling Pt formation on P25 TiO<sub>2</sub> during photodeposition. Their study investigated the role of methanol in the fabrication of Pt loaded on P25 TiO<sub>2</sub> for photocatalytic H<sub>2</sub> generation. Pt was deposited on TiO<sub>2</sub> using chloroplatinic acid (H<sub>2</sub>PtCl<sub>6</sub>) as a precursor in an aqueous solution with various methanol concentrations under 300 W Xe lamp illumination with an intensity of 124.6 mW cm<sup>-2</sup>.<sup>66</sup> It was found that the resulting H<sub>2</sub> production rate increased linearly with the vol% of methanol used in the precursor solution. Fig. 4 shows bright-field high-resolution transmission electron microscopy (HRTEM) images of the resulting Pt-loaded P25 TiO<sub>2</sub> NPs and the corresponding particle distributions. The dark spots in the bright-field HRTEM images can be associated with the Pt loading due to Z contrast. Fig. 4a-1 and a-2 exhibit the Pt-loaded P25 TiO<sub>2</sub> surfaces when 100 vol% methanol was used during the deposition.

When considering Z contrast, the small dark spots on the grey particles can be associated with highly dispersed small Pt NPs. Fig. 4b-1 and b-2 show the resulting Pt-loaded P25 TiO<sub>2</sub> when 20 vol% methanol was used during deposition. Comparing these images to those of a 100 vol% sample, it was observed that the overall dispersion of the Pt NPs has decreased, and the overall size of the Pt NPs increased. For the samples prepared in a 0 vol% methanol solution, highly dispersed dark spots can be seen in the resulting HRTEM images shown in Fig. 4c-1 and c-2. Here, the dispersion and size of the samples appear comparable to those of the 100% vol sample. Fig. 4d depicts a Pt nanoparticle on the P25 TiO<sub>2</sub> surface. Based on the structure of the crystallites present, it can be concluded that the Pt NPs grow at the interface between anatase and rutile crystallites, indicating no preferential substrate crystal phase. In fact, Jiang *et al.*<sup>66</sup> reported that the Pt NPs were deposited randomly across the anatase and rutile surfaces of P25 TiO<sub>2</sub>. The particle distribution of Pt particles can be extracted from

TEM images of particles with different vol% samples used during sample preparation, as shown in Fig. 4e. It can be observed that both 100 vol% and 0 vol% methanol lead to highly dispersed Pt NPs (mostly <2.5 nm), whereas 20 vol% methanol leads to larger Pt NPs (some >4 nm). Upon an increase in methanol from 20 vol% up to 100 vol%, a decrease in the overall particle size and an increase in the dispersion could be observed. This is consistent with the TEM images discussed above. The decrease in particle size and the increase in dispersion can be attributed to methanol acting as a hole scavenger, suppressing recombination in TiO<sub>2</sub> during the photodeposition and leading to electron-rich surfaces where metallic Pt can be deposited. At 0 vol%, non-metallic Pt compounds like PtO<sub>2</sub> and PtCl lead to high dispersion. Still, an increase in methanol concentration causes metallic Pt to be produced more frequently, initially leading to large metallic Pt NPs at low concentrations. The Pt loading shows more dispersion and a decrease in the size of particles as the methanol concentration increases. This leads to the conclusion that the photodeposition of Pt on P25 TiO<sub>2</sub> methanol drives both Pt reduction and its subsequent redispersion.

Over the years, numerous studies have been published based on the photodeposition of noble metals on P25 TiO<sub>2</sub> NPs for various applications (Table 3).<sup>22,30,46,53,57,58,66–68,70–73</sup> Investigation of these data concludes that mercury lamps and sometimes xenon lamps were preferentially used to perform the photodeposition reactions. Usually, an aqueous AgNO<sub>3</sub> solution is used as a precursor for the photodeposition of Ag NPs. However, different sacrificial agents can be used for specific purposes, such as varying particle sizes and surface coverages. Chlorine-based precursors such as H<sub>2</sub>PtCl<sub>6</sub> and HAuCl<sub>4</sub> solutions are commonly used to prepare Pt and Au NPs, respectively. These chlorine-based compounds are readily available and have high solubility in water.

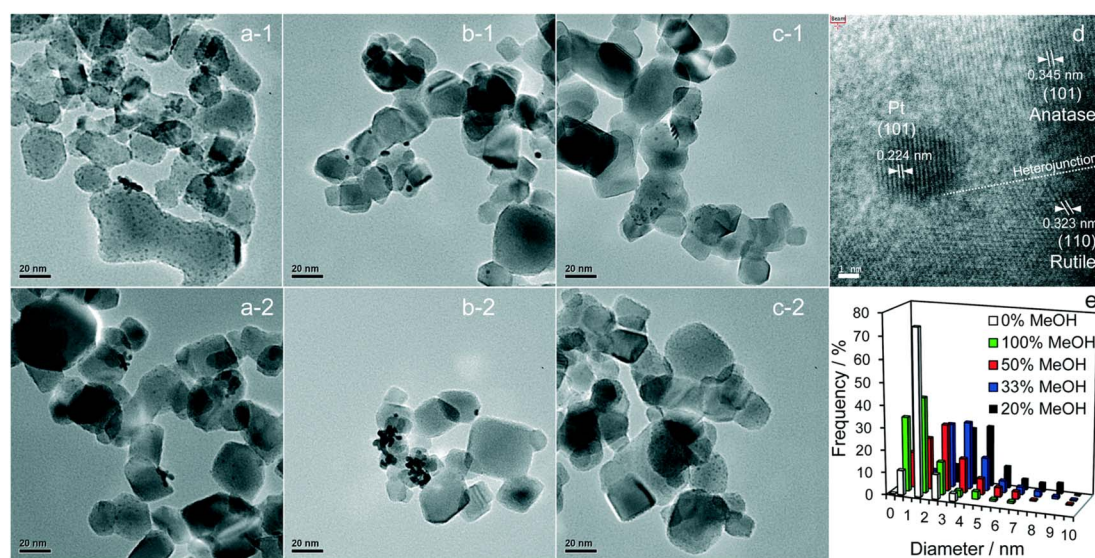


Fig. 4 Representative bright-field HRTEM images of (a-1 and a-2) 100%, (b-1 and b-2) 20%, and (c-1 and c-2) 0% MeOH with 1 wt% Pt/TiO<sub>2</sub>, and (d) an individual Pt metal nanoparticle at the interface between anatase and rutile crystallites. (e) Particle size distributions as a function of methanol concentration during PD. Adapted with permission from ref. 66. Copyright (2016) Royal Society of Chemistry (RSC).



**Table 3** Overview of different noble metal NPs photodeposited on TiO<sub>2</sub> NPs for various applications (the wavelength refers to the maximum wavelength of the emission spectrum of the respective light source)

Deposited noble metal	UV source and wavelength ( $\lambda$ )	Precursor molecule; additional agent	Possible applications	Reported in
Ag	Mercury arc lamp, 125 W 10.4 mW cm <sup>-2</sup> , $\lambda$ not given	AgNO <sub>3</sub> ; isopropanol	Photodegradation of salicylic acid	Bhardwaj <i>et al.</i> <sup>58</sup>
Ag	Xenon lamp, 300 W, $\lambda$ not given	AgNO <sub>3</sub> ; sodium hydrogen carbonate	Photocatalytic reduction of CO <sub>2</sub> with water	Hammad <i>et al.</i> <sup>53</sup>
Ag	Mercury lamp, 500 W, $\lambda = 365$ nm	AgNO <sub>3</sub> ; methanol	Not given	Ma <i>et al.</i> <sup>70</sup>
Ag	UV-A lamp, 40 W, $\lambda = 350$ –400 nm	[Ag(S <sub>2</sub> O <sub>3</sub> ) <sub>2</sub> ] <sup>3-</sup> in radiographic wastewater	Bacterial disinfection	Wahyuni <i>et al.</i> <sup>71</sup>
Ag and Pt	Mercury lamp, 200 W, $\lambda = 365$ nm	AgNO <sub>3</sub> K <sub>2</sub> PtCl <sub>4</sub> Trisodium citrate	Not given	Taing <i>et al.</i> <sup>57</sup>
Pd	Low-pressure mercury lamp, 250 W m <sup>-2</sup> , $\lambda$ not given	PdCl <sub>2</sub> ; methanol	Organic photodegradation reactions	Dadsetan <i>et al.</i> <sup>68</sup>
Pd	Low-pressure mercury lamp, 250 W m <sup>-2</sup> , $\lambda$ not given	PdCl <sub>2</sub> ; methanol, ethanol, ethylene glycol, and 1-isopropanol	Not given	Dadsetan <i>et al.</i> <sup>46</sup>
Bimetallic Pd–Au	Mercury lamp, 6 W, $\lambda = 254$ nm	Pd(C <sub>5</sub> H <sub>7</sub> O <sub>2</sub> ) <sub>2</sub> HAuCl <sub>4</sub> ·3H <sub>2</sub> O Acetonitrile	Selective oxidative esterification of methanol to form methyl formate	Colmenares <i>et al.</i> <sup>72</sup>
Pt	Super-pressure mercury lamp, 30 mW cm <sup>-2</sup> , $\lambda = 240$ –500 nm	H <sub>2</sub> PtCl <sub>6</sub> ; methanol	Photocatalytic H <sub>2</sub> evolution	Haselmann <i>et al.</i> <sup>30</sup>
Pt	Xenon lamp, 300 W, $\lambda$ not given	H <sub>2</sub> PtCl <sub>6</sub> ; methanol	Photocatalytic H <sub>2</sub> evolution	Jiang <i>et al.</i> <sup>66</sup>
Au and Pt	Mercury lamp, 0.15 W m <sup>-2</sup> , $\lambda = 365$ nm	HAuCl <sub>4</sub> H <sub>2</sub> PtCl <sub>6</sub> Isopropanol	Not given	Galeano <i>et al.</i> <sup>73</sup>
Au, Pt, and Rh	Mercury–xenon lamp, 200 W, $\lambda$ not given	AuCl <sub>3</sub> (Au <sub>2</sub> Cl <sub>6</sub> ) H <sub>2</sub> PtCl <sub>6</sub> ·6H <sub>2</sub> O RhCl <sub>3</sub> Methanol	Not given	Ohyama <i>et al.</i> <sup>22</sup>
Au, Pt, Rh, Pd, and Ag	High-pressure mercury arc lamp, $\lambda > 300$ nm	HAuCl <sub>4</sub> Colloidal Au nanoparticles Oxalic acid Other precursors not given	Water splitting without using any reagents under irradiation of visible light	Tanaka <i>et al.</i> <sup>67</sup>

**2.1.2. TiO<sub>2</sub> nanocrystals.** Nanocrystals (NCs) are aggregates of atoms that combine into a “cluster” and are less than 1  $\mu$ m in size. Typical sizes range between 10 and 400 nm.<sup>74</sup> TiO<sub>2</sub> nanocrystals have been extensively used in materials research, chemical engineering, and as quantum dots for biological imaging.<sup>75,76</sup> Synthesizing TiO<sub>2</sub> NCs with a high surface area is vital to maximizing the properties of the nanocrystals. Essentially, TiO<sub>2</sub> has three distinct crystallographic phases (anatase, rutile, and brookite) of which anatase and rutile (thermodynamically more stable forms) in the ratio of 70 : 30 have been utilized as excellent photocatalysts for photodecomposition of organic pollutants and solar-energy conversion due to their high photoactivity.<sup>77,78</sup> In general, TiO<sub>2</sub> has been shown to possess an anatase tetragonal bipyramidal polymorphic structure that mainly exposes the (101) planes, with a small percentage of the (001) facet based on Wulff construction.<sup>79</sup> Typically, anatase TiO<sub>2</sub> NPs have been mainly synthesized by wet chemical synthesis methods such as sol–gel,<sup>80–83</sup> micelle/reverse micelle,<sup>84</sup> and hydrothermal methods.<sup>85</sup> The sol–gel method proceeds with the hydrolysis of titanium(IV) alkoxide, followed by condensation.<sup>86</sup> In the micelle/reverse micelle method, TiO<sub>2</sub> nanocrystals are obtained by controlled micelle or reverse micelle formation by hydrolysis of a titanium alkoxide

precursor and then annealing the sample to induce crystallinity.<sup>84</sup> In the hydrothermal method, dehydration of an aqueous solution of titanium salt at high temperatures provides nanocrystals.<sup>87</sup> Liu *et al.*<sup>88</sup> utilized a two-step hydrothermal method to synthesize well-defined truncated tetragonal bipyramidal TiO<sub>2</sub> NCs having (001) facets exposed on the top/bottom surface and (101) on the side surface. Subsequently, Au–Pd alloy NPs with a fixed Au to Pd atomic ratio of 1 : 1 were immobilized on the pristine TiO<sub>2</sub> NCs *via* photodeposition that resulted in PD-Au<sub>1</sub>Pd<sub>1</sub> composition. Similarly, a reference sample of Au : Pd in a 1:1 ratio was prepared by ascorbic acid (AA) induced chemical reduction (*i.e.*, CR-Au<sub>1</sub>Pd<sub>1</sub>). By TEM analysis (Fig. 5a and e), Chen *et al.* showed that CR-Au<sub>1</sub>Pd<sub>1</sub> possessed some Au–Pd NPs of darker contrast evenly anchored on the (101) and (001) facets of the TiO<sub>2</sub> NCs, while the Au–Pd NPs of PD-Au<sub>1</sub>Pd<sub>1</sub> were specifically deposited on the (101) facets of the TiO<sub>2</sub> NCs. HR-TEM images of these NPs on CR-Au<sub>1</sub>Pd<sub>1</sub> and PD-Au<sub>1</sub>Pd<sub>1</sub> revealed clear lattice fringes with an interlayer spacing of 0.226 nm, corresponding to the (111) planes of a face-centered cubic (FCC) metal (Fig. 5b and f).<sup>90,91</sup>

Similarly, Chen *et al.*<sup>92</sup> used one-step *in situ* photodeposition to deposit different noble metals such as gold, silver, platinum, and palladium on TiO<sub>2</sub> nanocrystals (Fig. 6). The photocatalytic





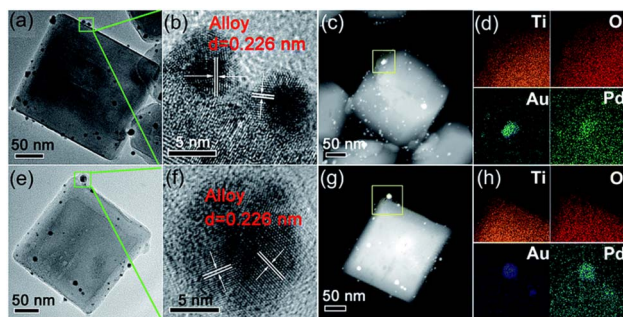


Fig. 5 Detailed morphology and composition analysis of two representative samples: (a–d) CR-Au<sub>1</sub>Pd<sub>1</sub> and (e–h) PD-Au<sub>1</sub>Pd<sub>1</sub>. (a and e) TEM images, (b and f) HR-TEM images, (c and g) HAADF-STEM images, and (d and h) corresponding EDX mapping of Ti, O, Au, and Pd, respectively. Adapted with permission from ref. 89. Copyright (2018) Royal Society of Chemistry (RSC).

activities of M–TiO<sub>2</sub> (M = Au, Ag, Pt, and Pd) samples were evaluated by the photocatalytic selective oxidation of benzyl alcohol. The noble metals were supported on hollow TiO<sub>2</sub> nanocrystals *via* the *in situ* photodeposition method.

Here, the deposition of Au, Ag, Pt, and Pd was achieved using chloroauric acid (HAuCl<sub>4</sub>), silver nitrate (AgNO<sub>3</sub>), hexachloroplatinic(IV) acid (H<sub>2</sub>PtCl<sub>6</sub>), and palladium(II) chloride (PdCl<sub>2</sub>) as the precursors, respectively. The TEM and HRTEM image analyses showed 2 wt% of noble NPs loaded on TiO<sub>2</sub>–H (Fig. 6). The results revealed the presence of spherical noble

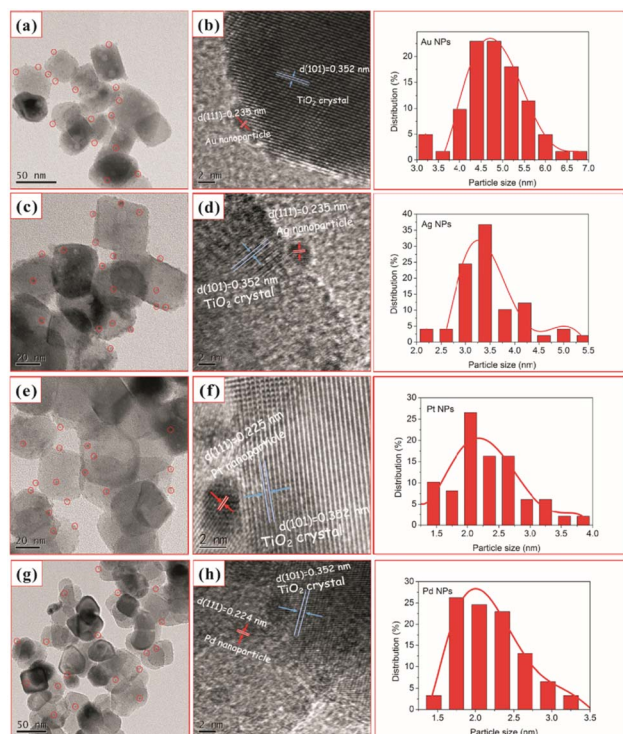


Fig. 6 TEM and HRTEM images of TiO<sub>2</sub>–H after loading with 2 wt% Au (a and b), Ag (c and d), Pt (e and f), and Pd (g and h) and (right) nanoparticle size distribution for the corresponding M–TiO<sub>2</sub> (M = Au, Ag, Pt, and Pd). Adapted with permission from ref. 92. Copyright (2017) Elsevier.

metal NPs on the surface of the TiO<sub>2</sub> support material for different M–TiO<sub>2</sub> hybrid nanostructures. As illustrated by the red circles in Fig. 6 (a, c, e, and g), Au, Ag, Pt, and Pd metal NPs were observed as dark spots uniformly decorated on TiO<sub>2</sub> nanocrystals. The large conglomerates of metal NPs on TiO<sub>2</sub> support were not observed. Notably, the photoreduction of Pt(IV) or Pd(II) ions formed smaller NPs (~2 nm) as compared to that of the solution consisting of the same amount of Au(III) or Ag(I) ions (NPs ranging from 4 to 5 nm). The larger size of Au NPs, compared to the Pd and Pt NPs, was attributed to a weaker metal support interaction in the case of Au with TiO<sub>2</sub>. As shown in the HRTEM images in Fig. 6 (b, d, f, and h), characteristic lattice fringes of 0.235, 0.235, 0.225, and 0.224 nm for Au, Ag, Pt, and Pd NPs were observed and indexed to the (111) plane of face-centered cubic structures.

## 2.2. 1D structures

**2.2.1. TiO<sub>2</sub> nanotubes.** An essential factor that dominates the photocatalytic performance and application of any loaded TiO<sub>2</sub> or unloaded TiO<sub>2</sub> photocatalyst is the effective surface area, which is significantly higher for NPs than for bulk samples. However, in applications, the NPs are either used in a suspension or immobilized by another processing step like sintering. This disadvantage is not present in TiO<sub>2</sub> nanotube arrays produced by an anodization process on a metallic Ti substrate. They provide a relatively large surface area, and the prepared nanotubes are attached to a substrate that provides immobilization for photocatalytic applications.<sup>93</sup> The process of anodization for producing TiO<sub>2</sub> nanotubes on a Ti substrate was first reported by Zwillinger *et al.* in 1999.<sup>94</sup> Fluoride in the electrolyte solution of the anodization process led to the self-organization of nanotubes instead of a continuous oxide layer in the anodization process. Since then, the TiO<sub>2</sub> nanotube production by using anodization was further optimized, and today, nanotubes of several 100 μm lengths and diameters between 10 nm and >200 nm can be grown by using this process.<sup>93</sup>

Lv *et al.* successively constructed Pt-loaded TiO<sub>2</sub> nanotube (TNT) arrays with a uniform distribution of Pt *via* photodeposition.<sup>95</sup> Fig. 7 schematically shows the fabrication process of Pt-loaded TiO<sub>2</sub> nanotubes. First, a TiO<sub>2</sub> nanotube array was produced by the well-known anodization process. A Ti foil was used as an anode, and it was oxidized in an electrolyte solution at 40 V for 8 h against a graphite cathode. The anodic oxidation of Ti led to the formation of TiO<sub>2</sub> nanotube arrays.

In the following step, photodeposition of Pt on the TiO<sub>2</sub> nanotubes was performed using aqueous solutions of H<sub>2</sub>PtCl<sub>6</sub> with different concentrations and illuminating the submerged

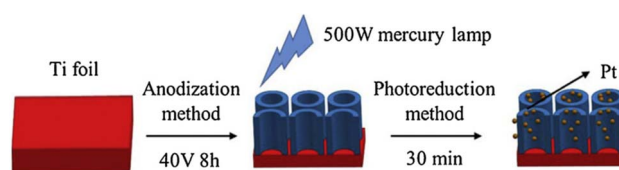


Fig. 7 Schematic of the fabrication process of Pt/TiO<sub>2</sub> NTAs. Adapted with permission from ref. 95. Copyright (2019) Elsevier.



nanotube array sample with a 500 W mercury lamp for 30 minutes. XPS measurements found that the resulting Pt deposits are most likely metallic. Moreover, UV-vis absorption spectra revealed that the highest visible absorption could be achieved at an initial  $\text{H}_2\text{PtCl}_6$  precursor concentration of  $3 \text{ mmol L}^{-1}$ , corresponding to the highest photodegradation rate of methyl orange.

Jia *et al.* used photodeposition of Ag on  $\text{TiO}_2$  nanotubes to prepare photocatalysts, which were used for the photoelectrocatalytic reduction of perchlorate under a bias potential and in the presence of the hole scavenger citric acid.<sup>96</sup> The  $\text{TiO}_2$  nanotubes were prepared by an anodization process similar to the method schematically shown in Fig. 8.

The Ag loading was carried out by the photoreduction of  $\text{AgNO}_3$  (volume ratio of ethanol/deionized water equal to 1 : 4) under UV illumination (light of intensity  $I = 3.5 \text{ mW cm}^{-2}$ ) for 30 minutes with continuous nitrogen purging. SEM images of the resulting photocatalyst are presented in Fig. 8. Bare  $\text{TiO}_2$  nanotubes are shown in Fig. 8a, and nearly no particles can be seen on their surface. A small number of particles are still present on the surface, which do not belong to Ag (supported by EDX analysis). Fig. 8b–d show the resulting Ag-loaded  $\text{TiO}_2$  nanotubes for 1, 2, and  $3 \text{ g L}^{-1}$  concentrations of initial  $\text{AgNO}_3$ , respectively. It was observed that the number of particles on the  $\text{TiO}_2$  nanotubes increased with increasing  $\text{AgNO}_3$  concentration. It was also noted that the average particle size increased with the increase in  $\text{AgNO}_3$  concentration from 9 nm to 20 nm and to 130 nm, respectively. From photoelectrocatalytic experiments, it was found that the sample shown in Fig. 8c, which was prepared with a  $2 \text{ g L}^{-1}$   $\text{AgNO}_3$  solution and showing a 0.84% Ag/ $\text{TiO}_2$  mass ratio, exhibits the highest perchlorate reduction rate.<sup>96</sup>

**2.2.2.  $\text{TiO}_2$  nanowires.** Compared with one-dimensional nanostructures of rods and tubes, titania nanowire (TNW) arrays have been confirmed to possess an advantage in charge separation over compact films,<sup>97</sup> which is vital for photocatalysts and photoanodes. TNWs have shown to be a promising photocatalyst because of their improved structural, surface, and optoelectronic properties.<sup>98</sup> Wang *et al.* and Mandal and Bhatlacharya studied Pt-modified TNWs and bare TNWs,

respectively, and found 5- and 2-fold higher photocatalytic activity than P25  $\text{TiO}_2$  for the degradation of methylene blue dye.<sup>99,100</sup>

Ren and Liu loaded PdAu alloyed NPs on  $\text{TiO}_2$  nanowires *via* a one-step photochemical deposition method, and the Pd/Au ratio in alloyed NPs could be adjusted by changing the  $\text{Pd}^{2+}/\text{Au}^{3+}$  ratio.<sup>101</sup> Reductants and surfactants were avoided in the whole synthesis process. To synthesize PdAu alloyed NPs with different Pd/Au ratios, 16 mL of  $\text{PdCl}_2$  (0.5 mM) solution in ethanol was mixed with a certain amount of  $\text{HAuCl}_4$  (10 mM) solution in ethanol. For comparison, the same procedure was modified to deposit Pd or Au NPs on  $\text{TiO}_2$  nanowires with 0.5 mM  $\text{PdCl}_2$  or  $\text{HAuCl}_4$  solution, respectively. After 24 h of hydrothermal growth,  $\text{TiO}_2$  nanowires were densely distributed on the Ti foil. One single nanowire marked with the red arrow line was selected to estimate its length. Although its two ends exceed the measurement region, its length still reached  $15 \mu\text{m}$ . As shown in the bottom-left inset in Fig. 9a, after UV irradiation for 30 min in  $\text{PdCl}_2$  solution, the color of the  $\text{TiO}_2$  nanowire film changed from milky white to black, which indicated the successful loading of Pd NPs on the  $\text{TiO}_2$  surface. As shown in Fig. 9a, a large amount of Pd NPs was loaded on the  $\text{TiO}_2$  surface, and the majority was 35–65 nm in diameter. A magnified SEM picture of a few Pd NPs indicated that a single nanoparticle on the nanowire comprised an agglomerate of many smaller NPs, as shown in the upper-left inset in Fig. 9a.

When  $\text{HAuCl}_4$  solution was used to deposit Au NPs under identical conditions, the as-synthesized Au nanostructures exhibited a lower density and wider size distribution than Pd NPs loaded NWs (Fig. 9b). It should be noted that their size obviously decreases along with the loading site changing from upper  $\text{TiO}_2$  nanowires to bottom ones. The mixed solution of  $\text{PdCl}_2$  and  $\text{HAuCl}_4$  was used to synthesize PdAu alloyed NPs on  $\text{TiO}_2$  nanowires. Fig. 9c shows the  $\text{Pd}_4\text{Au}$  alloyed NPs synthesized with a  $\text{Pd}^{2+}/\text{Au}^{3+} = 4$  ratio in precursor solutions. Except

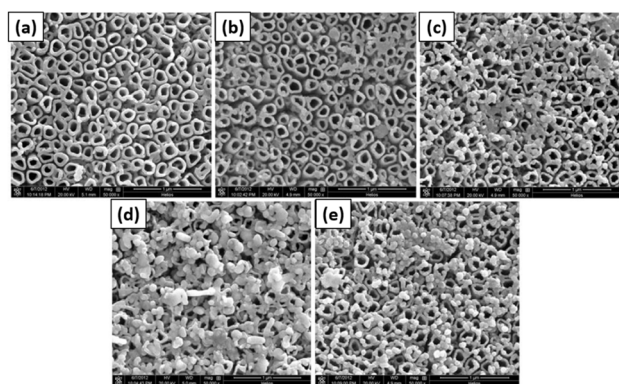


Fig. 8 SEM images of (a) TNTs, (b) Ag-TNTs-1, (c) Ag-TNTs-2, (d) Ag-TNTs-3 and used (e) Ag-TNTs-2. Adapted with permission from ref. 96. Copyright (2016) Elsevier.

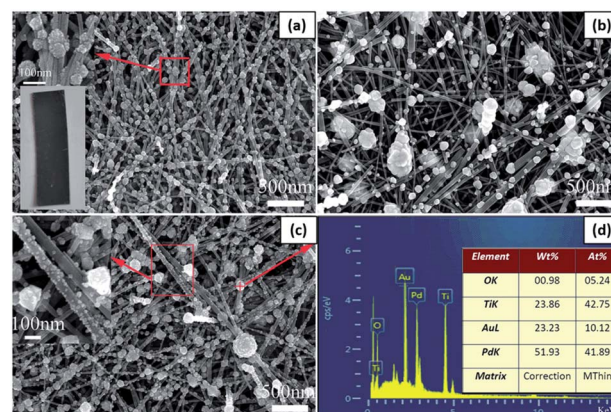


Fig. 9 SEM pictures of (a)  $\text{Pd@TiO}_2$ , (b)  $\text{Au@TiO}_2$  and (c)  $\text{Pd}_4\text{Au@TiO}_2$ . (d) The EDS spectrum for the particle in panel (c) marked with a red "+" symbol. The upper-left and bottom-left insets in panel (a) are the enlarged SEM image of a few NPs and the photograph of  $\text{Pd@TiO}_2$ , respectively. The inset in panel (c) is the enlarged SEM image for the marked region with a red box. The inset in panel (d) lists the elemental distribution in  $\text{Pd}_4\text{Au@TiO}_2$ . Adapted with permission from ref. 101. Copyright (2016) Royal Society of Chemistry (RSC).



for a few NPs with a diameter of about 100 nm, a large number of smaller NPs were loaded on the  $\text{TiO}_2$  surface, as shown in the inset in Fig. 9c. Fig. 9d shows the corresponding energy dispersive spectroscopy (EDS) spectrum of the single particle marked with the “+” symbol in Fig. 9c. Among the four elements, the O and Ti elements came from the  $\text{TiO}_2$  substrate, and Pd and Au came from the photodeposited NPs. The Pd/Au ratio in alloyed NPs was 4.14, which is almost the same as the  $\text{Pd}^{2+}/\text{Au}^{3+}$  ratio in the precursor solution.

Park *et al.* demonstrated the development of Au-NP decorated ZnO- $\text{TiO}_2$  core-shell NWs *via* a two-step process; the preparation of ZnO- $\text{TiO}_2$  core-shell NWs was carried out using chemical vapor deposition (CVD), and decoration of Au-NPs was done on the ZnO- $\text{TiO}_2$  core-shell NWs using photodeposition (PD).<sup>102</sup> A schematic representation of ZnO, ZT, and ZTA NWs heterostructure synthesis is shown in Fig. 10. Primarily, a thin layer of carbon was coated on a Si-wafer. Then, well-aligned ZnO NWs were grown on the carbon-coated Si-wafer. Subsequently, a thin layer of  $\text{TiO}_2$  shell was deposited on the ZnO NWs core. Finally, Au-NPs were decorated on the ZnO- $\text{TiO}_2$  core-shell NWs heterostructure by the PD method. It was observed that decoration of plasmonic Au-NPs enhanced the photocurrent density and photoconversion efficiency of as-prepared ZnO- $\text{TiO}_2$  core-shell NWs due to increased visible light absorption, efficient electron extraction from Au-NPs due to the Schottky barrier, effective charge separation at multi-interface and transportation through 1D NWs. This study demonstrates that the plasmonic Au-NPs decorated on the ZnO- $\text{TiO}_2$  core-shell NWs improve the PEC performance.

### 2.3. 2D structures

**2.3.1.  $\text{TiO}_2$  thin films.** As discussed in the introduction, the particle geometry, size, and crystallinity of  $\text{TiO}_2$  are crucial to its photoactivity.<sup>103–106</sup> The surface chemistry of  $\text{TiO}_2$  largely depends on the surface area, morphology, and exposed crystal planes.<sup>105</sup> In general, the  $\text{TiO}_2$  NPs (P25) have been practically recognized as the “golden standard” photocatalyst because of their effectiveness in pollutant degradation (organic dyes and other pollutants) in water.<sup>107</sup> However,  $\text{TiO}_2$  thin films are more suitable for water treatment and environmental remediation applications such as air purification.<sup>108</sup> On the other hand,

$\text{TiO}_2$  thin films have a very inadequate surface area that hampers the effective photocatalytic degradation of organic pollutants.<sup>109</sup> Hence, different strategies have been proposed to improve the volume-to-surface area ratio of  $\text{TiO}_2$  thin films for high photocatalytic activity.  $\text{TiO}_2$  thin films can be prepared by various methods such as physical vapor deposition (PVD) (including thermal evaporation, reactive sputtering, ion or electron beam evaporation), chemical vapor deposition (CVD) techniques, as well as wet chemical deposition methods such as sol-gel, solvothermal, dip-coating, spin-coating, and spray coating.<sup>39,110–115</sup> As a factor of cost and ease of up-scaling, wet chemical methods are favored particularly for outdoor applications (self-cleaning textiles or exterior walls of buildings) of  $\text{TiO}_2$ -based coatings. However, such methods usually require a secondary process, such as drying and high annealing temperature, to achieve stable and crystalline  $\text{TiO}_2$  layers, which is crucial for high photocatalytic performance.<sup>116</sup>

Alternatively, sputtering and evaporation techniques have been developed to produce columnar or sculptured thin films with enhanced porosity.<sup>110</sup> Suzuki *et al.* reported that surface reaction enhanced the efficiency of obliquely deposited  $\text{TiO}_2$  thin films with different columnar geometrical shapes, including zigzag, cylindrical, and helical morphologies.<sup>117</sup> More so, Goossens *et al.* reported a fractal (“forest-like”) 3D  $\text{TiO}_2$  thin film.<sup>118</sup> The choice of deposition method not only plays a role in the thin film structure but is also a contributing factor to the photocatalytic activity of the thin film.<sup>119</sup> Another approach to enhance the photocatalytic activity of  $\text{TiO}_2$  thin films is the decoration by metallic nanostructures *via* photodeposition. The decoration of  $\text{TiO}_2$  thin films with noble metals such as Au, Ag, Pd, and Pt has been shown to exhibit excellent absorption properties due to the local surface plasmon resonance (LSPR) activities.<sup>120</sup> Using Au and Ag for decorating  $\text{TiO}_2$  thin films has led to red-shifted and increased LSPR, which reduces charge recombination at the surface of  $\text{TiO}_2$ , yielding an improved overall photocatalytic performance. Furthermore, those metal clusters are also electron acceptors and enhance charge separation, and there can be competing processes.

Tossi *et al.*<sup>121</sup> explained the photodeposition of Pt NPs on  $\text{TiO}_2$  thin films that were grown *via* ALD (Fig. 11a). They mainly reported that the photodeposition parameters influence the control and prediction of the deposited nanoparticles' size, density, and loading. Fig. 11c summarizes the SEM images of different samples under different reaction conditions. On the top, the  $\text{TiO}_2$  deposited FTO-coated glass, samples 5 (see the corresponding parameters in Fig. 11b) and 8 (see the corresponding parameters in Fig. 11b) after the platinum photodeposition are shown with white parts as NPs. On the bottom, three SEM images of sample 7 (see the corresponding parameters in Fig. 11b) are given. They indicated that platinum oxide is visible even at low magnifications, and only a few metallic particles are visible at higher magnifications, which is a characteristic of platinum oxide. This work analyzed the photodeposition method for metal NPs from liquid precursors on ALD-grown films.

Recently, a highly active Au nanocluster (NC) fabrication on a  $\text{TiO}_2$  thin film surface by the photodeposition method was

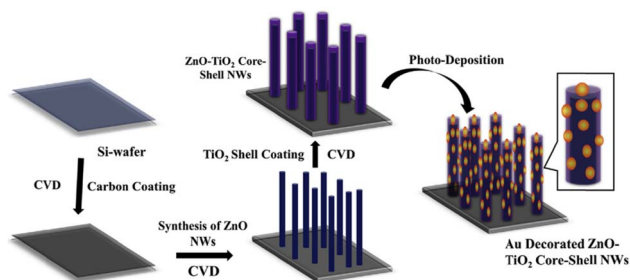
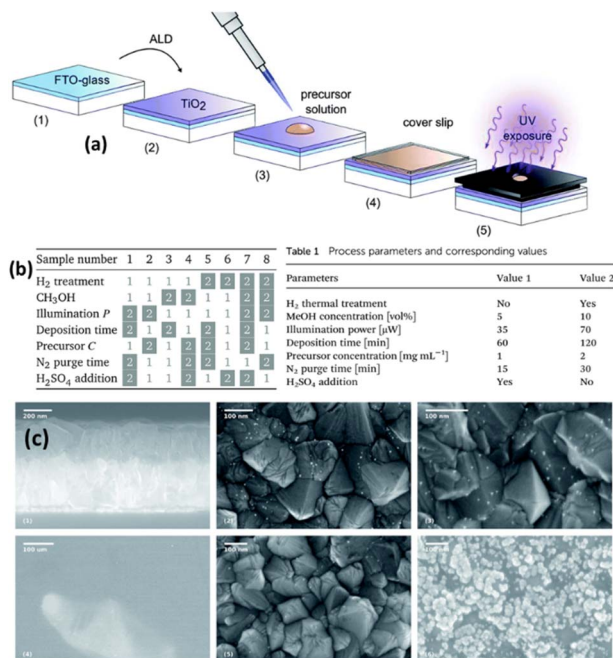


Fig. 10 Schematic representation of development of Au-NP decorated ZnO- $\text{TiO}_2$  core-shell NWs on the Si-wafer. Adapted with permission from ref. 102 Copyright (2018) American Chemical Society (ACS).





**Fig. 11** (a) Sample preparation and exposure: the H<sub>2</sub> thermal treatment, when applied, takes place between steps (2) and (3). The illuminated area of the sample is 0.15 cm<sup>2</sup> out of 5.5 cm<sup>2</sup>. (b) The eight combinations of parameters for each sample: the white boxes refer to value 1 in Table 1 (inset), while the gray boxes refer to value 2. (c) SEM micrographs: on the top, from left to right, are the section of the FTO-coated glass after the TiO<sub>2</sub> deposition, and the surfaces of samples 5 and 8 after the platinum photodeposition, the nanoparticles shown in white. On the bottom part of the figure, three micrographs of sample 7 show the clear-colored platinum oxide well visible already at low magnification and higher magnifications of the darker area, where a few metallic particles are visible, and of the clear area, with the characteristic growth patterns for platinum oxide. Adapted with permission from ref. 121 (2019) Royal Society of Chemistry (RSC).

demonstrated.<sup>122</sup> The surface coverage of TiO<sub>2</sub> by Au NCs was found to be controlled by changing the solvent type and the illumination time. Higher photocatalytic performance was observed at a low surface coverage due to the high optical absorption of TiO<sub>2</sub> at UV wavelengths. As indicated in morphological analysis (HIM images in Fig. 12a–d), different solvents (acetone, isopropanol, and 1-hexanol) were investigated to obtain the impacts on the photocatalytic depositions of Au NCs on TiO<sub>2</sub>. It was observed that water, among the other solvents, resulted in the lowest surface coverage value by Au NCs on TiO<sub>2</sub> films. In contrast, the highest density of Au nano-clusters was achieved by a mixture of 1-hexanol–water as a solvent, as illustrated in Fig. 12e.

As mentioned in the previous sections, the photocatalytic deposition method gives strong adhesion between deposited noble metals and the semiconductor surface. It is essential to use these hybrid nanostructures for various applications, especially for continuous water systems. The photocatalytic deposition approach can also pattern micro-/nanostructures without any stabilizer or surfactant, as shown in Fig. 13.<sup>20</sup> Fig. 13a illustrates the photocatalytic deposition of hierarchical Au needle clusters (HAuNCs) on a highly active TiO<sub>2</sub> thin film

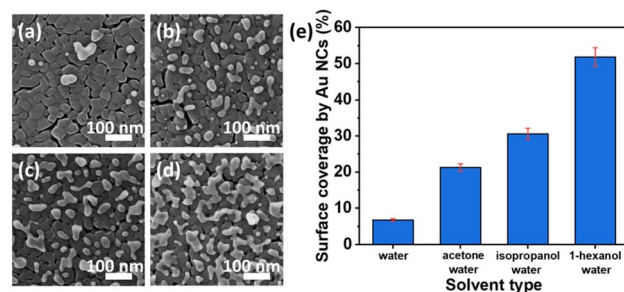


**Fig. 12** HIM images of Au NCs deposited onto TiO<sub>2</sub> in (a) water, (b) acetone–water (v/v: 20/80), (c) isopropanol–water (v/v: 20/80), and (d) 1-hexanol–water (v/v: 20/80) mixtures. (e) Surface coverage (%) by Au NCs deposited with different solvents. Adapted with permission from ref. 122. Copyright (2020) American Chemical Society (ACS).

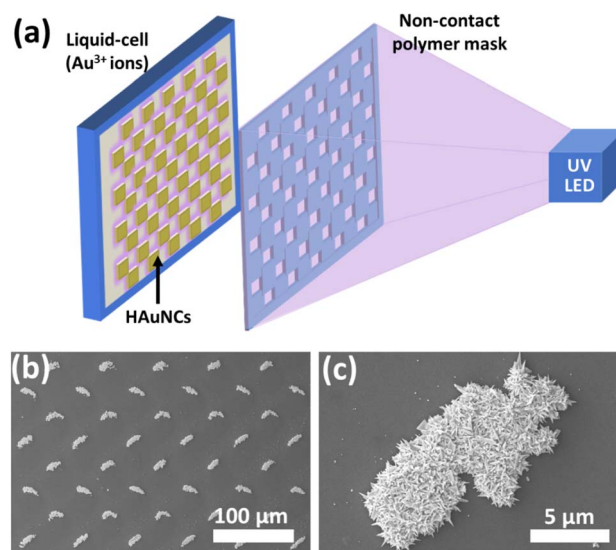


**Fig. 13** (a) Schematic representation of photocatalytic patterning of the TiO<sub>2</sub> thin film with HAuNCs using a noncontact polymer mask. SEM images of (b) periodic HAuNC arrays and (c) a single HAuNC. Adapted with permission from ref. 20. Copyright (2018) Wiley.

surface. The non-contact polymer mask is located between the UV LED and the thin film sample. The TiO<sub>2</sub> thin film surface can be selectively illuminated to reduce Au ions as metallic Au in only these illuminated areas (Fig. 13b and c). The rest remains empty due to UV LED non-illumination. The photocatalytic deposition approach is practical for preparing various shapes and patterned noble metal structures on semiconductors for well-desired applications (catalysis, plasmonic, and biomedical technologies).

### 3 Concluding remarks and future perspectives of photocatalytic deposition

In recent years, extensive research on noble metal–TiO<sub>2</sub> nanostructures has demonstrated their crucial role in various

applications such as water splitting, self-cleaning, CO<sub>2</sub> reduction, and water remediation. The structure of the noble metal–TiO<sub>2</sub> composite is critical in determining its photocatalytic properties. Various studies in the literature on preparing noble metals with different shapes and sizes exist. However, obtaining good adhesion between the noble metal and TiO<sub>2</sub> surface is still challenging. Photodeposition is a promising approach to obtain well-desired noble metal structures on TiO<sub>2</sub> surfaces with strong adhesion. Noble metal NPs can be quickly grown on the TiO<sub>2</sub> surface under light exposure. However, numerous parameters (pH, temperature, precursor, electron sacrificial agent, *etc.*) affect the size and distribution of the deposited particles. In addition to these parameters, the interaction between solution and OD, 1D, and 2D morphologies might differ due to surface tension forces, drastically affecting the uniformity of the deposited metal nanostructures. This review focused on a few significant types of TiO<sub>2</sub> morphologies (0D: NPs and nanocrystals; 1D: nanotubes and nanowires; and 2D: thin films) to better understand the photocatalytic deposition process. Based on available data, more fundamental research on different TiO<sub>2</sub> morphologies is still needed to develop highly active photocatalytic structures for specific applications. Hopefully, this review can inspire multidisciplinary research interest in precisely tailoring TiO<sub>2</sub> morphology to study in various applications.

## Data availability

No primary research results, software or code have been included and no new data were generated or analysed as part of this review.

## Conflicts of interest

There are no conflicts to declare.

## Acknowledgements

Open access funding enabled and organized by Projekt DEAL.

## References

- 1 A. P. Alivisatos, *Science*, 1996, **271**, 933–937.
- 2 X. Liu, J. Iocozzia, Y. Wang, X. Cui, Y. Chen, S. Zhao, Z. Li and Z. Lin, *Energy Environ. Sci.*, 2017, **10**, 402–434.
- 3 J. Shondo, S. Veziroglu, T. Tjardts, J. Fiutowski, S. Schröder, Y. K. Mishra, T. Strunskus, H. Rubahn, F. Faupel and O. C. Aktas, *Adv. Mater. Interfaces*, 2022, **9**, 2102126.
- 4 Y. C. Yen, P. H. Chen, J. Z. Chen, J. A. Chen and K. J. Lin, *ACS Appl. Mater. Interfaces*, 2015, **7**, 1892–1898.
- 5 M. Tomás-Gamasa and J. L. Mascareñas, TiO<sub>2</sub>-Based Photocatalysis at the Interface with Biology and Biomedicine, *ChemBioChem*, 2020, **21**, 294.
- 6 S. Liu, M. D. Regulacio, S. Y. Tee, Y. W. Khin, C. P. Teng, L. D. Koh, G. Guan and M. Y. Han, *Chem. Rec.*, 2016, **16**, 1965–1990.
- 7 J. Shondo, S. Veziroglu, T. Tjardts, T. Bin Sarwar, Y. K. Mishra, F. Faupel and O. C. Aktas, *Small*, 2022, **18**, 2203861.
- 8 K. C. F. Leung, S. Xuan, X. Zhu, D. Wang, C. P. Chak, S. F. Lee, W. K. W. Ho and B. C. T. Chung, *Chem. Soc. Rev.*, 2012, **41**, 1911–1928.
- 9 T. S. Ahmadi, Z. L. Wang, T. C. Green, A. Henglein and M. A. El-Sayed, *Science*, 1996, **272**, 1924–1925.
- 10 D. Ma, *Noble Met. Oxide Hybrid Nanoparticles Fundam. Appl.*, 2019, pp. 3–6.
- 11 S. Yoda, K. Ohtake, Y. Takebayashi, T. Sugeta, T. Sako and T. Sato, *J. Mater. Chem.*, 2000, **10**, 2151–2156.
- 12 A. V. Rane, K. Kanny, V. K. Abitha and S. Thomas, *Methods for Synthesis of Nanoparticles and Fabrication of Nanocomposites*, Elsevier Ltd, 2018.
- 13 T. Liu, W. Chen, T. Huang, G. Duan, X. Yang and X. Liu, *J. Mater. Sci.*, 2016, **51**, 6987–6997.
- 14 J. G. Kang and Y. Sohn, *J. Mater. Sci.*, 2012, **47**, 824–832.
- 15 N. P. Dasgupta, C. Liu, S. Andrews, F. B. Prinz and P. Yang, *J. Am. Chem. Soc.*, 2013, **135**, 12932–12935.
- 16 Y. Busby and J. J. Pireaux, *J. Electron Spectrosc. Relat. Phenom.*, 2014, **192**, 13–18.
- 17 Annu, A. Ali and S. Ahmed, in *Handbook of Ecomaterials*, ed. L. M. T. Martínez, O. V. Kharissova and B. I. Kharisov, Springer International Publishing, Cham, 2019, pp. 2281–2325.
- 18 J. Shondo, S. Veziroglu, D. Stefan, Y. K. Mishra, T. Strunskus, F. Faupel and O. C. Aktas, *Appl. Surf. Sci.*, 2020, 147795.
- 19 A. Abedini, A. R. Daud, M. Azmi, A. Hamid, N. K. Othman, E. Saion, M. A. A. Hamid, N. K. Othman and E. Saion, *Nanoscale Res. Lett.*, 2013, **8**, 1–10.
- 20 S. Veziroglu, M. Z. Ghorri, M. Kamp, L. Kienle, H. G. Rubahn, T. Strunskus, J. Fiutowski, J. Adam, F. Faupel and O. C. Aktas, *Adv. Mater. Interfaces*, 2018, **5**, 1–7.
- 21 M. Sadowsky and P. D. Payne, *J. Electrochem. Soc.*, 1958, **105**, 105.
- 22 J. Ohyama, A. Yamamoto, K. Teramura, T. Shishido and T. Tanaka, *ACS Catal.*, 2011, **1**, 187–192.
- 23 K. Wenderich and G. Mul, *Chem. Rev.*, 2016, **116**, 14587–14619.
- 24 M. A. Fox and M. T. Dulay, *Chem. Rev.*, 1993, **93**, 341–357.
- 25 O. Carp, C. L. Huisman and A. Reller, *Prog. Solid State Chem.*, 2004, **32**, 33–177.
- 26 C. P. C. V. Bernardo, R. A. M. Lameirinhas, J. P. de Melo Cunha and J. P. N. Torres, *A Revision of the Semiconductor Theory from History to Applications*, Springer International Publishing, 2024, vol. 6.
- 27 W. Guo, J. Huang and W. D. Wei, in *Plasmonic Catalysis*, Wiley, 2021, pp. 295–322.
- 28 W. Schottky, *Naturwissenschaften*, 1938, **26**, 843.
- 29 H. Dong, G. Zeng, L. Tang, C. Fan, C. Zhang, X. He and Y. He, *Water Res.*, 2015, **79**, 128–146.
- 30 G. M. Haselmann and D. Eder, *ACS Catal.*, 2017, **7**, 4668–4675.
- 31 L. Kavan, *J. Solid State Electrochem.*, 2024, **28**, 829–845.





- 32 V. Mansfeldova, M. Zlamalova, H. Tarabkova, P. Janda, M. Vorokhta, L. Piliari and L. Kavan, *J. Phys. Chem. C*, 2021, **125**, 1902–1912.
- 33 M. Zlamalova, V. Mansfeldova, H. Tarabkova, H. Krysova and L. Kavan, *J. Solid State Electrochem.*, 2023, **27**, 1935–1943.
- 34 C. Lattyak, K. Gehrke and M. Vehse, *J. Phys. Chem. C*, 2022, **126**, 13929–13935.
- 35 Q. Huang, T. Gao, F. Niu, D. Chen, Z. Chen, L. Qin, X. Sun, Y. Huang and K. Shu, *Superlattices Microstruct.*, 2014, **75**, 890–900.
- 36 S. Garcia-Segura and E. Brillas, *J. Photochem. Photobiol., C*, 2017, **31**, 1–35.
- 37 F. O. F. Business, A. Arts, G. Chidichimo, L. Filippelli, E. L. Pierre, B. Zhou, B. Shi, D. Jin, X. Liu, F. Jiang, W. C. H. Choy, X. Li, D. Zhang, J. Cheng, A. K. Gaharwar, N. A. Peppas, A. Khademhosseini, A. Nouioua, D. Barkat, M. L. Petrus, J. Schlipf, C. Li, T. P. Gujar, N. Giesbrecht, P. Müller-Buschbaum, M. Thelakkat, T. Bein, S. Hüttner, P. Docampo, L. Shaabani, R. Singh, S. Dutta, A. Tampieri, G. Celotti, E. Landi, C. A. Mirkin, R. L. Letsinger, R. C. Mucic and J. J. Storhoff, *Fuel*, 2015, **111**, 607–620.
- 38 S. M. Gupta and M. Tripathi, *Chin. Sci. Bull.*, 2011, **56**, 1639–1657.
- 39 A. Vahl, S. Veziroglu, B. Henkel, T. Strunskus, O. Polonskyi, O. C. Aktas and F. Faupel, *Materials*, 2019, **12**, 2840.
- 40 S. Veziroglu, J. Hwang, J. Drewes, I. Barg, J. Shondo, T. Strunskus, O. Polonskyi, F. Faupel and O. C. Aktas, *Mater. Today Chem.*, 2020, **16**, 100251.
- 41 S. Kalantzis, S. Veziroglu, T. Kohlhaas, C. Flörke, Y. K. Mishra, J. Wiltfang, Y. Açil, F. Faupel, O. C. Aktas and A. Gülses, *RSC Adv.*, 2020, **10**, 28935–28940.
- 42 C. Renz, *Helv. Chim. Acta*, 1921, **4**, 961–968.
- 43 C. Renz, *Helv. Chim. Acta*, 1932, **15**, 1077–1084.
- 44 W. C. Clark and A. G. Vondjidis, *J. Catal.*, 1965, **4**, 691–696.
- 45 B. Kraeutler and A. J. Bard, *J. Am. Chem. Soc.*, 1978, **100**, 4317–4318.
- 46 S. Dadsetan, S. Baghshahi and S. M. M. Hadavi, *J. Australas. Ceram. Soc.*, 2018, **54**, 383–388.
- 47 F. Zhang, J. Chen, X. Zhang, W. Gao, R. Jin, N. Guan and Y. Li, *Langmuir*, 2004, **20**, 9329–9334.
- 48 J. M. Herrmann, J. Disdier and P. Pichat, *J. Phys. Chem.*, 1986, **90**, 6028–6034.
- 49 N. A. Jani, C. Haw, W. Chiu, S. A. Rahman, P. Khiew, Y. Lim, R. Abd-Shukor and M. A. A. Hamid, *J. Nanomater.*, 2020, **2020**, 1–11.
- 50 E. M. See, C. Tossi, L. Hällström and I. Tittonen, *ACS Omega*, 2020, **5**, 10671–10679.
- 51 M. C. Hidalgo, J. J. Murcia, J. A. Navío and G. Colón, *Appl. Catal., A*, 2011, **397**, 112–120.
- 52 L. G. Devi and R. Kavitha, *Appl. Surf. Sci.*, 2016, **360**, 601–622.
- 53 A. Hammad, A. Anzai, X. Zhu, A. Yamamoto, D. Ootsuki, T. Yoshida, A. EL-Shazly, M. Elkady and H. Yoshida, *Catal. Lett.*, 2020, **150**, 1081–1088.
- 54 D. Ferrah and P. Tieu, *ACS Appl. Nano Mater.*, 2020, **3**, 5855–5861.
- 55 Y. J. Hwang, C. Hahn, B. Liu and P. Yang, *ACS Nano*, 2012, **6**, 5060–5069.
- 56 F. Sieland, J. Schneider and D. W. Bahnemann, *Phys. Chem. Chem. Phys.*, 2018, **20**, 8119–8132.
- 57 J. Taing, M. H. Cheng and J. C. Hemminger, *ACS Nano*, 2011, **5**, 6325–6333.
- 58 S. Bhardwaj, D. Sharma, P. Kumari and B. Pal, *Opt. Mater.*, 2020, **106**, 109975.
- 59 Y. Lee, E. Kim, Y. Park, J. Kim, W. H. Ryu, J. Rho and K. Kim, *J. Mater.*, 2018, **4**, 83–94.
- 60 B. Gupta, A. A. Melvin, T. Matthews, S. Dash and A. K. Tyagi, *Renewable Sustainable Energy Rev.*, 2016, **58**, 1366–1375.
- 61 C. Wang, H. Liu, Y. Liu, G. He and C. Jiang, *Appl. Surf. Sci.*, 2014, **319**, 2–7.
- 62 T. Ohno, K. Sarukawa, K. Tokieda and M. Matsumura, *J. Catal.*, 2001, **203**, 82–86.
- 63 B. Ohtani, O. O. Prieto-Mahaney, D. Li and R. Abe, *J. Photochem., Photobiol. A*, 2010, **216**(2–3), 179–182.
- 64 R. I. Bickley, T. Gonzalez-Carreno, J. S. Lees, L. Palmisano and R. J. D. Tilley, *J. Solid State Chem.*, 1991, **92**, 178–190.
- 65 B. Ohtani, O. O. Prieto-Mahaney, D. Li and R. Abe, *J. Photochem. Photobiol., A*, 2010, **216**, 179–182.
- 66 Z. Jiang, Z. Y. Zhang, W. Shangguan, M. A. Isaacs, L. J. Durndell, C. M. A. Parlett and A. F. Lee, *Catal. Sci. Technol.*, 2016, **6**, 81–88.
- 67 A. Tanaka, K. Teramura, S. Hosokawa, H. Kominami and T. Tanaka, *Chem. Sci.*, 2017, **8**, 2574–2580.
- 68 S. Dadsetan, S. Baghshahi, F. Farshidfar and S. M. M. Hadavi, *Ceram. Int.*, 2017, **43**, 9322–9326.
- 69 A. Sclafani and J. M. Herrmann, *J. Photochem. Photobiol., A*, 1998, **113**, 181–188.
- 70 J. Ma, X. Guo, Y. Zhang and H. Ge, *Chem. Eng. J.*, 2014, **258**, 247–253.
- 71 E. T. Wahyuni, R. Roto, D. Novarita, K. P. Suwondo and B. Kuswandi, *J. Environ. Chem. Eng.*, 2019, **7**, 103178.
- 72 J. C. Colmenares, P. Lisowski, D. Łomot, O. Chernyayeva and D. Lisovyskiy, *ChemSusChem*, 2015, **8**, 1676–1685.
- 73 L. Galeano, S. Valencia, J. M. Marin, G. Restrepo, J. A. Navío and M. C. Hidalgo, *Mater. Res. Express*, 2019, **6**, 1050d9.
- 74 V. P. Chavda, in *Applications of Targeted Nano Drugs and Delivery Systems*, Elsevier, 2019, pp. 69–92.
- 75 B. Dubertret, *Science*, 2002, **298**, 1759–1762.
- 76 X. Gao, Y. Cui, R. M. Levenson, L. W. K. Chung and S. Nie, *Nat. Biotechnol.*, 2004, **22**, 969–976.
- 77 O. D'Hennezel and D. F. Ollis, *Helv. Chim. Acta*, 2001, **84**, 3511–3518.
- 78 K. Nagaveni, G. Sivalingam, M. Hegde and G. Madras, *Appl. Catal., B*, 2004, **48**, 83–93.
- 79 M. Lazzeri, A. Vittadini and A. Selloni, *Phys. Rev. B: Condens. Matter Mater. Phys.*, 2001, **63**, 155409.
- 80 S. S. El-Deen, A. M. Hashem, A. E. Abdel Ghany, S. Indris, H. Ehrenberg, A. Mauger and C. M. Julien, *Ionics*, 2018, **24**, 2925–2934.
- 81 Y. T. Kim, Y. S. Park, H. Myung and H. K. Chae, *Colloids Surf., A*, 2008, **313–314**, 260–263.
- 82 B. K. Mutuma, G. N. Shao, W. D. Kim and H. T. Kim, *J. Colloid Interface Sci.*, 2015, **442**, 1–7.



- 83 Y. Yao, T. Zhai, C. Liu, Y. Guan, J. Zhang, D. Xu and J. Luo, *Ceram. Int.*, 2015, **41**, 14740–14747.
- 84 M. H. Nateq and R. Ceccato, *Adv. Mater. Sci. Eng.*, 2019, **2019**, 1–14.
- 85 F. Wang, Z. Shi, F. Gong, J. Jiu and M. Adachi, *Chin. J. Chem. Eng.*, 2007, **15**, 754–759.
- 86 F. Sayilkan, M. Asiltürk, H. Sayilkan, Y. Önal, M. Akarsu and E. Arpaç, *Turk. J. Chem.*, 2005, **29**, 697–706.
- 87 S. Mathew, A. Kumar Prasad, T. Benoy, P. P. Rakesh, M. Hari, T. M. Libish, P. Radhakrishnan, V. P. N. Nampoori and C. P. G. Vallabhan, *J. Fluoresc.*, 2012, **22**, 1563–1569.
- 88 C. Liu, X. Han, S. Xie, Q. Kuang, X. Wang, M. Jin, Z. Xie and L. Zheng, *Chem.-Asian J.*, 2013, **8**, 282–289.
- 89 Q. Chen, X. Chen, M. Fang, J. Chen, Y. Li, Z. Xie, Q. Kuang and L. Zheng, *J. Mater. Chem. A*, 2019, **7**, 1334–1340.
- 90 X. Chen, Z. Cai, X. Chen and M. Oyama, *J. Mater. Chem. A*, 2014, **2**, 5668–5674.
- 91 Z.-L. Wang, J.-M. Yan, Y.-F. Zhang, Y. Ping, H.-L. Wang and Q. Jiang, *Nanoscale*, 2014, **6**, 3073.
- 92 Y. Chen, Y. Wang, W. Li, Q. Yang, Q. Hou, L. Wei, L. Liu, F. Huang and M. Ju, *Appl. Catal., B*, 2017, **210**, 352–367.
- 93 I. Paramasivam, H. Jha, N. Liu and P. Schmuki, *Small*, 2012, **8**, 3073–3103.
- 94 V. Zwilling, E. Darque-Ceretti, A. Boutry-Forveille, D. David, M. Y. Perrin and M. Aucouturier, *Surf. Interface Anal.*, 1999, **27**, 629–637.
- 95 J. Lv, H. Gao, H. Wang, X. Lu, G. Xu, D. Wang, Z. Chen, X. Zhang, Z. Zheng and Y. Wu, *Appl. Surf. Sci.*, 2015, **351**, 225–231.
- 96 Y. Jia, L. Ye, X. Kang, H. You, S. Wang and J. Yao, *J. Photochem. Photobiol., A*, 2016, **328**, 225–232.
- 97 B. Li, J.-M. Wu, T.-T. Guo, M.-Z. Tang and W. Wen, *Nanoscale*, 2014, **6**, 3046.
- 98 I. S. Grover, R. C. Prajapat, S. Singh and B. Pal, *Sol. Energy*, 2017, **144**, 612–618.
- 99 C. Wang, L. Yin, L. Zhang, N. Liu, N. Lun and Y. Qi, *ACS Appl. Mater. Interfaces*, 2010, **2**, 3373–3377.
- 100 S. S. Mandal and A. J. Bhattacharyya, *Talanta*, 2010, **82**, 876–884.
- 101 S. Ren and W. Liu, *J. Mater. Chem. A*, 2016, **4**, 2236–2245.
- 102 J. Park, P. R. Deshmukh, Y. Sohn and W. G. Shin, *J. Alloys Compd.*, 2019, **787**, 1310–1319.
- 103 T. Ohno, S. Y. Lee and Y. Yang, *Rare Met.*, 2015, **34**, 291–300.
- 104 E. Bae, N. Murakami and T. Ohno, *J. Mol. Catal. A: Chem.*, 2009, **300**, 72–79.
- 105 T. Ohno, T. Higo, H. Saito, S. Yuajn, Z. Jin, Y. Yang and T. Tsubota, *J. Mol. Catal. A: Chem.*, 2015, **396**, 261–267.
- 106 T. Ohno, K. Sarukawa and M. Matsumura, *New J. Chem.*, 2002, **26**, 1167–1170.
- 107 D. Chen, Y. Cheng, N. Zhou, P. Chen, Y. Wang, K. Li, S. Huo, P. Cheng, P. Peng, R. Zhang, L. Wang, H. Liu, Y. Liu and R. Ruan, *J. Cleaner Prod.*, 2020, **268**, 121725.
- 108 D. Li, H. Haneda, S. Hishita and N. Ohashi, *Chem. Mater.*, 2005, **17**, 2596–2602.
- 109 J. Rodriguez, M. Gómez, J. Lu, E. Olsson and C. G. Granqvist, *Adv. Mater.*, 2000, **12**, 341–343.
- 110 M. Z. Ghorri, S. Veziroglu, B. Henkel, A. Vahl, O. Polonskyi, T. Strunskus, F. Faupel and O. C. Aktas, *Sol. Energy Mater. Sol. Cells*, 2018, **178**, 170–178.
- 111 V. G. Bessergenev, R. J. F. Pereira, M. C. Mateus, I. V. Khmelinskii, D. A. Vasconcelos, R. Nicula, E. Burkel, A. M. Botelho Do Rego and A. I. Saprykin, *Thin Solid Films*, 2006, **503**, 29–39.
- 112 J. Yu, X. Zhao and Q. Zhao, *Thin Solid Films*, 2000, **379**, 7–14.
- 113 Y. G. Seo, M. A. Kim, H. Lee and W. Lee, *Sol. Energy Mater. Sol. Cells*, 2011, **95**, 332–335.
- 114 A. Ranga Rao and V. Dutta, *Sol. Energy Mater. Sol. Cells*, 2007, **91**, 1075–1080.
- 115 D. Dastan, S. L. Panahi and N. B. Chaure, *J. Mater. Sci.: Mater. Electron.*, 2016, **27**, 12291–12296.
- 116 J. G. Yu, H. G. Yu, B. Cheng, X. J. Zhao, J. C. Yu and W. K. Ho, *J. Phys. Chem. B*, 2003, **107**, 13871–13879.
- 117 M. Suzuki, T. Ito and Y. Taga, *Appl. Phys. Lett.*, 2001, **78**, 3968–3970.
- 118 A. Goossens, E. L. Maloney and J. Schoonman, *Chem. Vap. Deposition*, 1998, **4**, 109–114.
- 119 B. Henkel, T. Neubert, S. Zabel, C. Lamprecht, C. Selhuber-Unkel, K. Rätzke, T. Strunskus, M. Vergöhl and F. Faupel, *Appl. Catal., B*, 2016, **180**, 362–371.
- 120 S. Veziroglu, M. Ullrich, M. Hussain, J. Drewes, J. Shondo, T. Strunskus, J. Adam, F. Faupel and O. C. Aktas, *Surf. Coat. Technol.*, 2020, **389**, 125613.
- 121 C. Tossi, L. Hällström, J. Selin, M. Vaelma, E. See, J. Lahtinen and I. Tittonen, *J. Mater. Chem. A*, 2019, **7**, 14519–14525.
- 122 S. Veziroglu, A.-L. Obermann, M. Ullrich, M. Hussain, M. Kamp, L. Kienle, T. Leißner, H.-G. Rubahn, O. Polonskyi, T. Strunskus, J. Fiutowski, M. Es-Souni, J. Adam, F. Faupel and O. C. Aktas, *ACS Appl. Mater. Interfaces*, 2020, **12**, 14983–14992.

